Research Square

Preprints are preliminary reports that have not undergone peer review.
They should not be considered conclusive, used to inform clinical practice,
or referenced by the media as validated information.

A Liquid Phase to Destabilize Nanoconfined $LiBH_4$/LiH: the LiCl/KCl Eutectic

Ignacio Ariel Garanzini
Consejo Nacional de Investigaciones Científicas y Técnicas (CONICET) and Centro Atómico Bariloche (CNEA)

Pierre Arneodo Larochette
Consejo Nacional de Investigaciones Científicas y Técnicas (CONICET) and Centro Atómico Bariloche (CNEA)

Aurelien Gasnier
aurelien.gasnier@cab.cnea.gov.ar

Consejo Nacional de Investigaciones Científicas y Técnicas (CONICET) and Centro Atómico Bariloche (CNEA)

Research Article

Keywords: Hydrogen Storage, Mesoporous carbon, LiBH4, Nanoconfinement, Eutectics

Posted Date: September 10th, 2026

DOI: https://doi.org/10.21203/rs.3.rs-10882005/v1

License: This work is licensed under a Creative Commons Attribution 4.0 International License.
Read Full License

Additional Declarations: No competing interests reported.

Abstract

We present the decoration of a mesoporous carbon matrix with a LiCl/KCl eutectic by hand milling or incipient wetness impregnation. Nitrogen isotherms indicated that the latter favoured the salt impregnation of the pores. Electron microscopy revealed cubic nanoparticles ranging from 100 to 1000 nm covering the matrix. Powder X-ray diffractometry confirmed the presence of LiCl and KCl crystals. The characteristic melting peak of the LiCl/KCl eutectic was detected at 354 ºC by differential scanning calorimetry. The LiCl/KCl decorated matrices were then melt-impregnated with $LiBH_4$. Nitrogen isotherms indicated limited LiCl/KCl impact on $LiBH_4$ pore filling, beneficial for wet-impregnated matrices but detrimental to ground matrices. SEM observations revealed partially melted nanocrystals at the matrix surface. Calorimetry of the decorated materials exhibited a broader and less intense $LiBH_4$ decomposition peak shifted toward higher temperatures (348 ºC), while no melting peak was observed and the transition peak shifted sharply toward lower temperatures (70 ºC). Powder X-ray diffractometry evidenced the disappearance of KCl and suggested the formation of $LiK(BH_4)_2$ after impregnation with $LiBH_4$. Volumetric studies revealed that the onset of hydrogen release was shifted toward lower temperatures for wet-impregnated samples, but higher temperatures were required to finish the decomposition of ground samples. No effect on the system´s reversibility was observed. XRD and DSC could not demonstrate the presence of the LiH/LiCl/KCl eutectic after cycling. However, SEM observation revealed the formation of needle-shaped crystals after decomposition.

Introduction

Clean energy is essential for replacing fossil fuels, whose combustion leads to depletion and negative environmental impact [1]. As a carbon-free energy carrier, hydrogen is pivotal for the implementation of renewable energies [2]. The discovery of abundant fossil hydrogen reserves makes it even more attractive, as it may promote the energy grid transition toward a carbon-free model [3]. However, its low density limits its use, even in high-pressure systems [4, 5]. Lithium borohydride ($LiBH_4$) offers high hydrogen capacities in the solid state [6–9]. Nevertheless, strong ionic and covalent bonds [10] promote high decomposition temperatures (> 450°C) [11]. Furthermore, the generation of toxic diborane (B_2H_6) and of thermally stable $Li_2B_{12}H_{12}$ intermediate limits its reversibility [12].

Its performance is improved by other hydrides [13, 14], metals [13, 15], oxides [16], halides [17], and electron-donating/withdrawing heteroatoms [18]. Reducing particle size lowers its decomposition temperature by overcoming certain kinetic limitations [19]. However, particle sintering (~ 275 ºC) restrains cyclability [10]. Nanoconfinement of $LiBH_4$ lowers decomposition temperatures by more than 100 degrees [20, 21], prevents the liberation of diborane [22], and avoids sintering. But shrinking pore size increases the scaffold's dead mass, reducing the material's final capacity [23]. Si-matrices [24] present a catalytic behavior [9] but lower reversibility [25], while lighter C-matrices [26] offer numerous functionalization opportunities [27]. Graphene wrapping [28] and nanocages [29] are appealing because

they minimize matrix mass. The freed-up mass allows doping with other elements, paving the way for synergies [30, 31].

Such synergetic destabilization promoted significant, but insufficient, improvements in nanoconfined $LiBH_4$ [32–35]. Reversibility remains limited by [36] kinetics, chemical sinks (closoboranes), gas-phase element loss (B_2H_6), and physical separation of reactive species [12]. Several studies have addressed specific limitations of $LiBH_4$ (via destabilization [14], catalysis [37], or nanoconfinement [22]), but its reversibility has received less attention than its decomposition temperature [38]. The melting of $LiBH_4$ promotes boron doping of carbon defects, which improves its wetting of the carbon matrix. Unfortunately, B-doping also promotes the expulsion of LiH from the pores [39–41]. While nanoconfined $LiBH_4$ behaves as an ionic liquid at moderate temperatures [24, 42], LiH remains solid up to high temperatures. Thus, the segregation of the static solid phases of LiH and B compromises the system´s cyclability [41].

Mesoporous carbons were doped with graphene [23], nitrogen [27], and metallic nanoparticles [32, 43] to lower the dehydrogenation temperature of nanoconfined $LiBH_4$. Yet, even though carbon defects [23], Lewis bases [27], and/or acids [32] could potentially retain $LiBH_4$ degradation products, reversibility was not satisfactorily improved. Ni nanoparticles yielded the most encouraging results, yet are still far from practical application [32]. Furthermore, although NiB crystals improved reversibility, their formation implies that a different approach is needed to address boron availability and phase separation.

Recently, a metallic liquid phase was proposed to promote LiH(s)/B(s) interaction. By manual grinding, Ga nanodroplets decorated a mesoporous carbon matrix, lowering the $LiBH_4$ decomposition temperature by 25°C without improving reversibility [44]. Likely, the solubility of ionic LiH was negligible in metallic liquid gallium.

Given the ionic-liquid nature of nanoconfined $LiBH_4$, which governs its physicochemical and functional properties [24, 45, 46], its further destabilization by another liquid phase seemed attractive. As the ionic nature of LiH appeared to limit the usefulness of a metallic liquid phase, we devised that the LiCl/KCl eutectic may destabilize it or even promote its fusion. Indeed, the LiH/LiCl/KCl eutectic melts at 341 ºC [47].

Materials and methods

2.1. Synthesis of Materials.

2.1.1. Chemicals.

All chemicals were employed as received, without purification. Formaldehyde (40%) was supplied by Biopack (Buenos Aires, Argentina). Resorcinol (98.5%) was purchased from Cicarelli (San Lorenzo, Argentina). Sodium carbonate decahydrate (99.99%) was provided by Timper. Every hydride material was

handled within a glovebox to avoid air contact (content of oxygen and water < 5 ppm). $LiBH_4$ (Sigma-Aldrich, 90%) was milled before use.

2.1.2. Wet Synthesis.

The resorcinol-formaldehyde sols were prepared with a mixture of water (5.43 g), resorcinol (13.05 g), formaldehyde (19.52 g), and sodium carbonate (71.9 mg). After a quick dissolution of any solid part by mechanical stirring, the sols were poured into a polypropylene bottle. It was screw-tapped and allowed to rest for 24 hours. Then it was heated to 50 ºC for 24 h, then to 90 ºC for 72 h. The resins were washed at RT with acetone (3 additions of 10 ml, 24 h resting), then dried in the hood for 5 days.

Incipient wetness impregnation of the grinded matrix was performed prior to activation (see below). The LiCl and KCl salts were placed in an Erlenmeyer then were dissolved with methanol. The black carbon powder was added and placed under ultra sonication for 30 min. The suspension was agitated overnight, then the solvents were removed by rotary evaporation at 50 ºC.

2.1.3. Solid-State Synthesis.

The red resins were broken into smaller pieces (approx. 1 cm^3) and pyrolyzed at 800°C (3 ºC/min to 600 ºC, 1 h dwell, 3 ºC/min to 800 ºC, 5 h dwell, cooling to RT at 3 ºC/min), affording black chunks. Milling was performed with five stainless balls in an 80 cm^3 milling chamber filled with argon, using a P6 Pulverisette planetary device. $LiBH_4$ (1.5 g) was milled at 400 rpm, with a reverse sequence of 10 min milling and 10 min pause (15 cycles). The carbon matrix (1.5 g) was milled at 200 rpm with a reverse sequence of 1 min milling and 1 min pause (5 cycles). The black carbon powder R^0 (or its wet-impregnated ${}^{w}R_E^0$ counterpart) was activated at 400°C under reduced pressure for 5 h before introduction in the glovebox. The carbon matrix was decorated with LiCl/KCl in a 6:4 mol ratio by manual grinding (${}^{g}R_E^0$) in an agate mortar.

The porous materials (decorated or not) were manually mixed with $LiBH_4$ in the glovebox for 30 min using a mortar and pestle at 56 vol.%, according to the total volume (Gurvich) considering a density of 0.67 g/cm^3 for the hydride.

2.1.4. Melt Impregnation.

$LiBH_4$ impregnation was performed at 300°C under 60 bar H_2 for 30 min, affording the respective filled matrices: non decorated (R^{56}) and decorated (with LiCl/KCl eutectic) by grinding (${}^{g}R_E^{56}$) or wet-impregnation (${}^{w}R_E^{56}$). Once the system cooled back to RT, two options were taken: (i) the sample's hydrogen capacity was directly evaluated using a modified Sieverts-type device and (ii) the impregnated sample was stored in the glovebox for subsequent characterizations.

2.2. Material Characterization.

Textural parameters of the samples were determined using a Micromeritics ASAP 2020 analyzer. Approximately 0.1 g of sample was placed in a round-bottomed tube with a dead volume. Surface cleaning was performed by heating at 300 ºC under vacuum overnight (the temperature was limited to 150°C after impregnation or cycling). N_2 adsorption/desorption isotherms were collected at − 196°C after the dry system was precisely weighed. The surface area and pore-size distribution were obtained using the Brunauer–Emmett–Teller (BET) and Barrett–Joyner–Halenda (BJH) models, respectively. The surface area was determined using at least 5 points with P/P_0 ranging from 0.05 to a value determined by the Kei-Rouquerol criterion, affording positive C values. The total pore volume was determined by the Gurvich method at $P/P_0 = 0.975$. The micropore volume and the external surface were estimated using the t-plot method employing the standard reference t-curve for carbonaceous materials (carbon black) for $0.1 < P/P_0 < 0.5$.

Morphological analyses of the samples were performed by scanning electron microscopy (SEM, Zeiss, Crossbeam 340). The powders were dispersed over carbon tape. Elemental analyses of the materials were also performed by energy-dispersive X-ray spectroscopy (EDS) on SEM.

X-ray powder diffraction (XRPD) was realized with a special Kapton-walled air-tight chamber filled in a glovebox, and the trace was recorded on a Bruker D8 ADVANCE apparatus using Cu Kα radiation.

The thermal desorption behaviour of the samples was studied by differential scanning calorimetry (DSC, TA q2000 calorimeter), heating at 5°C/min to 400 ºC under argon flow (122 mL/min). To minimize air-contact, closed aluminium sampler were prepared within the glovebox and placed in an air-tight container. For impregnated samples the heat flow was normalized using a mass of material corresponding to 1 mg of $LiBH_4$. Before impregnation or after cycling the sample mass corresponded to the same amount of matrix (i.e. it would have contained 1 mg of $LiBH_4$ if impregnated or if not cycled).

Hydrogen sorption kinetic measurements were obtained using modified Sieverts equipment coupled with a mass flow controller to maintain constant pressure. The samples were placed in a stainless reactor, within an autoclave connected to the Sieverts device. Dehydrogenation curves were obtained by heating at 5°C/min up to 400°C with a hydrogen back pressure of 0.5 ± 0.1 bar. The rehydrogenation curves were measured at 400°C for 10 hours under an initial hydrogen pressure of 60 bars. The amount of absorbed/desorbed hydrogen is expressed as $H_2/LiBH_4$ mass ratio. It was determined with a relative error of ± 5%.

In the ensuing discussion, the samples are presented according to the following abbreviations: non-decorated resin (R), LiCl/KCl (20 vol.% of the Gurvich volume) decorated resin (R_E). $LiBH_4$ filling is indicated with an exposing number as vol.% (R^0 is the empty matrix, R^{56} is the matrix filled at 56 vol.%). Samples submitted to a cycle of dehydrogenation-rehydrogenation-dehydrogenation are indicated with a “c” prefix.

Results

3.1. LiCl/KCl-decorated matrix.

Sol-gel synthesis, followed by pyrolysis at 800 ºC, afforded the free resorcinol-formaldehyde matrix (R^0). The nitrogen isotherm of R^0 (Fig. 1A) exhibited a total pore volume of 0.62 cm^3/g, with a majority of mesopores (0.45 cm^3/g) and a non-negligible micropore amount (0.17 cm^3/g). To avoid overloading the matrix, we attributed 20% of the total pore volume (0.12 cm^3 per g of R) to the LiCl/KCl eutectic mixture, and 56% (0.35 cm^3 per g of R) to $LiBH_4$. R^0 was decorated with LiCl/KCl (6:4 mol.) by incipient wetness impregnation ($^wR_E{}^0$) and manual grinding ($^gR_E{}^0$). Relevant textural data are summarized in Table 1. The nitrogen isotherms of the decorated matrices exhibited a notable loss of the total pore volume (0.47 ± 0.01 cm^3/g). If the pore remained empty, the added salt mass (0.25 g per g of R) would increase the matrix density, reducing the total pore volume to 0.50 cm^3/g. If all the salt impregnated the pores, the combined effect of density and filling should lower the available pore volume to 0.40 cm^3/g. Experimentally, the actual pore volume of $^wR_E{}^0$ (0.46 cm^3/g) corresponds to an intermediate situation, with two-thirds of the salt remaining outside of the pores. Importantly, the micropores are not filled at all (0.13 cm^3/g), while the mesopores are partially filled (0.33 cm^3/g). In other words, two-thirds of the salt remained at the surface of the matrix, the micropores were not filled, while half of the expected mesopore filling occurred. Regarding $^gR_E{}^0$, the Gurvich volume of ^gR_E is a bit lower than expected if no filling occurred, but the difference is relatively small, so experimental uncertainty should be considered. Intuitively, grinding should promote pore filling less than incipient wetness impregnation, as confirmed experimentally by the higher $^gR_E{}^0$ Gurvich regarding $^wR_E{}^0$. Another important point is that the size of the average mesopore remained constant (7.8 nm) after decoration with LiCl and KCl, implying that pore filling did not occur radially.

Table 1

Textural parameters of R, $^{w}R_E$, and $^{g}R_E$ matrices, before impregnation, after filling with $LiBH_4$ 56 vol%, and after cycle dehydrogenation.

Sample	S_{BET} [a]	S_{mes} [b]	S_u [c]	V_G [d]	V_{mes} [e]	V_u [f]	d [j]
	cm^2/g			cm^3/g			nm
R^0	650	240	410	0.62	0.45	0.17	7.8
$^{g}R_E^0$	460	190	270	0.48	0.35	0.13	7.8
$^{w}R_E^0$	500	175	325	0.46	0.33	0.13	7.8
R^{56}	110	105	5	0.23	0.23	0	7.8
$^{g}R_E^{56}$	65	60	5	0.13	0.13	0	7.8
$^{w}R_E^{56}$	70	65	5	0.15	0.15	0	7.4
c-R^{56}	150	150	0	0.32	0.32	0	7.6
c-$^{g}R_E^{56}$	135	125	10	0.26	0.26	0	7.4
c-$^{w}R_E^{56}$	115	110	5	0.24	0.24	0	7.4

Values determined by [a] BET, [b] t-plot (V_{ext}), [c] S_{meso}-S_{BET}, [d] Gurvich, [e] V_{tot}-V_{micro}, [f] t-plot, [j] BJH.

After filling R^0 at 56 vol.% with $LiBH_4$ (Fig. 1B), the expected pore volume due to $LiBH_4$ mass (0.23 g $LiBH_4$ per gram of R^0) and volume (0.35 cm^3 per gram of R^0) should decrease to 0.22 cm^3/g. Experimental data (Table 1) are very close to this value, suggesting that very little $LiBH_4$ remains outside of the matrix. Regarding the decorated matrices, $LiBH_4$ filling should lead to a pore volume of 0.18 cm^3/g for $^{g}R_E^{56}$ and 0.17 cm^3/g for $^{w}R_E^{56}$. The experimental difference is not negligible, especially for $^{g}R_E^{56}$ (0.13 cm^3/g). It should be noted that, while the Gurvich volume of the decorated free matrices is higher for the ground one ($^{g}R_E^0$), filling reverses it. While experimental uncertainty should not be overlooked, the significant difference in pore size (7.4 nm for $^{w}R_E^{56}$ versus 7.8 nm for its ground counterpart) may imply different filling mechanisms, justifying the observed Gurvich volume variations. A constant pore diameter suggests axial filling, while a decrease in pore diameter suggests radial filling. Thus, the presence of LiCl/KCl within the pores of $^{w}R_E^0$ might interact with $LiBH_4$, altering pore filling. After filling, a higher-than-expected Gurvich volume suggests some $LiBH_4$ remains at the surface of the matrix; conversely, a lower value suggests pore clogging (empty pores are inaccessible to the N_2 adsorbate

because they are tapped). These clues converge, suggesting that wet impregnation promotes the presence of LiCl/KCl within the pores, thus preventing their clogging by $LiBH_4$ via radial filling.

Scanning Electron Microscopy revealed cubic structures of varied sizes (100–1000 nm) over $^{w}R_E^0$ (Fig. 2A). These structures were uniformly distributed over the carbon shards and from one to another (see Fig. S1 and S2). EDS mapping exhibited differences in K and Cl repartition, implying that some LiCl and KCl crystals were physically separated (see Fig. S2). While cubic structures were observed before impregnation, the flow of molten $LiBH_4$ affected those agglomerates, suggesting interactions (Fig. 2B and Fig. S3). It should be noted that melt impregnation is performed at 300 ºC, below the melting points of LiCl (610 ºC), KCl (770 ºC), or LiCl-KCl (352 ºC). Interestingly, EDS mapping reveals that Cl distribution is less defined after impregnation, suggesting that some LiCl and/or KCl migrate within the matrix due to the $LiBH_4$ flux (see Fig. S4).

All the diffractograms exhibited two broad bands at 2θ = 20 and 44º, corresponding to the amorphous carbon matrix (Fig. 3). $^{w}R_E^0$ and $^{g}R_E^0$ exhibited the distinctive LiCl (30.0, 34.9, 50.1, 59.5º) and KCl (28.4, 40.6, 50.1, 58.8º) patterns (Fig. 3A). After impregnation (Fig. 3B), a peak at 12.7º appeared with each powder, which can be attributed to $LiBH_4$. It should be reminded that the nanoconfinement of $LiBH_4$ reduces drastically the long-range order of its crystals, implying that XRD display weak or no $LiBH_4$ peaks [20]. While the peaks of LiCl remain, the peaks of KCl disappeared, suggesting an interaction between this species and $LiBH_4$. It can correspond to the cationic exchange of K for Li from KCl to LiCl. Indeed, while the intensity of the LiCl peaks increased, the $^{w}R_E^0$ trace displays two broad peaks at 14º and 17º, attributable to the formation of the $LiK(BH_4)_2$ species [48–50]. This implies that after $LiBH_4$ impregnation, no crystalline KCl remains.

Differential Scan Calorimetry (DSC) of the decorated matrices exhibited a peak at 354 ºC, which can be attributed to the melting of the LiCl/KCl eutectic (Fig. 4A) [47]. R^{56} displays the typical broad peaks of nanoconfined $LiBH_4$: orthorhombic-hexagonal transition around 106 ºC, fusion at 250 ºC, and decomposition at 337 ºC (Fig. 4B). After impregnation, the decorated matrices does not display the melting of the LiCl/KCl eutectic, while the three $LiBH_4$ typical peaks softened and shifted: a weak peak at 71 ºC may be attributed to the transition of nanoconfined species; two badly defined waves (at 228 and 301 ºC) could relate to their fusion; the decomposition peak is shifted toward higher temperatures at 348 ºC. The peaks at 71, 301 and 348 ºC may relate to the formation of the $LiK(BH_4)_2$ species, while the peak at 228 ºC is the only indication that can be related to nanoconfined $LiBH_4$ [48–50].

The volumetric study of the impregnated materials (Fig. 5A) shows that each sample liberated 14 wt% H_2 relative to the initial mass of $LiBH_4$. While the DSC of $^{g}R_E^{56}$ and $^{w}R_E^{56}$ exhibit higher decomposition peaks than R^{56}, the release of H_2 appears similar in each sample. Certain discrepancies between DSC and volumetric studies may arise owing to differences in gas conditions (DSC is performed with a strong Ar flow, effectively reducing the H_2 counter pressure to 0 bar, while volumetric studies are performed

under 0.4 < P_{H2} < 0.6 bar) [43, 44]. Interestingly, the onset dehydrogenation temperature was improved in the wet-impregnated matrix (the temperature was lowered by 12 °C to reach 1% of liberated H_2 in $^{w}R_E^{56}$), while the ground matrix displayed slower H_2 liberation at higher temperatures. Similarly, Martinez et al. evidenced the destabilizing effect of LiH toward the decomposition of $LiBH_4$, lowering the onset H_2 liberation temperature [41]. Here, this effect might relate to the nanoconfined LiCl and/or its improving effect toward $LiBH_4$ impregnation. Our materials exhibited similar reversibility, suggesting the LiH/LiCl/KCl eutectic might not form or does not improve it (Fig. 5A).

The samples were newly characterized after the dehydrogenation-rehydrogenation-dehydrogenation cycle. The cycled materials (c-R^{56}, c-$^{g}R_E^{56}$ and c-$^{w}R_E^{56}$) exhibited similar nitrogen isotherms (Fig. 1C). In each case, pore size and volume increased after cycling due to the ejection of LiH from the pores [39–41]. Microscopic observations of cycled $^{w}R_E^{56}$ (Fig. 2C and Fig. S5) revealed the formation of an acicular structure, with some remnant of its original cubic crystals. Notably, these needles are too thin to allow elemental mapping and vanish after a few electron-beam passes. At this stage, Cl and K seem dispersed throughout the material (see Fig. S6). Diffraction analysis (Fig. 3C) shows no new peak attributable to these needles, but the peaks at 12.7°, 14.1° and 17° have disappeared from the c-$^{w}R_E^{56}$ diffractogram. Furthermore, the characteristic LiCl peaks are less intense in c-$^{w}R_E^{56}$, whereas they retain their intensity on the c-$^{g}R_E^{56}$ trace. After cycling, no signal was observed by DSC. If the absence of $LiBH_4$ peaks is explained by its prior decomposition, the absence of any peak around 341 °C indicates the absence of the LiCl/KCl/LiH eutectic [47]. It can be explained by the physical separation between those salts, their nanoconfinement, or the formation of other species. Ill-defined waves are observable around 205 and 325 °C.

Conclusions

We decorated a mesoporous carbon matrix (R) with LiCl/KCl by manual grinding ($^{g}R_E$) and incipient wetness impregnation ($^{w}R_E$). Nitrogen isotherms indicated that LiCl/KCl incipient wetness impregnation induced better nanoconfinement of $LiBH_4$. Cubic structures were observed by SEM, related to LiCl and KCl by diffractometry. $LiBH_4$ melt-impregnation affected these structures, as the cubic structures exhibited a molten morphology by microscopy while their traces showed no KCl crystals. XRD of $^{w}R_E$ showed peaks attributable to $LiK(BH_4)_2$, which were absent from $^{g}R_E$. DSC demonstrated the presence of LiCl/KCl eutectics in the free-decorated matrices. Once impregnated, $^{g}R_E^{56}$ and $^{w}R_E^{56}$ displayed flattened transition, fusion, and decomposition peaks while the LiCl/KCl fusion peak disappeared. Calorimetry demonstrated that decorating the matrices increased the decomposition temperature by 11 °C. Volumetric studies showed that the onset decomposition temperature was lowered by 12 °C in $^{w}R_E^{56}$, while $^{g}R_E^{56}$ required higher temperatures to complete H_2 release. After cycling, the wet-impregnated samples showed less intense LiCl peaks on XRD traces, while DSC could not confirm the existence of a

LiH/LiCl/KCl eutectic. Given that LiCl/KCl wet impregnation demonstrated some advantages towards $LiBH_4$ nanoconfinement, a distinct matrix or an optimized impregnation method may be considered.

Abbreviations

BET
Brunauer–Emmet–Teller (model)
BJH
Barrett–Joyner–Halenda (model)
R: resorcinol-formaldehyde matrix.

Declarations

Author Contribution

I.G. is a PhD student on the subject of liquid phase effects over nanoconfined LiBH4. He is so the main specialist of the article, and performed all the experimental work and treatment. This justifies its position as first author.P.A. and A.G. are his thesis codirector and director. They prepared, presented and financed the thesis and are in charge of scientific assessement of I.G. They cured the data and guided I.G. through this work. This justifies their presence as coauthors.A. G. prepared the manuscript integrally, from data interpretation, conception, all the writings of the article, with correction and submission. This justifies his position as last author and corresponding author. P.A. and I.G. participed in the revision of the article.All the authors have published experience in the presented experimental methods and analysis. P.A. displays great amount of work on hydrides in general, A.G. on nanconfined LiBH4 in particular, while I.G. presented a work on the effect on liquid phase over nanoconfined LiBH4, which is an original and new investigation line.

Acknowledgement

The authors acknowledge the expertise and dedication of Carlos Bertoli and Bernardo Pentke during SEM observations.

Data Availability

All data supporting the findings of this study are available within the paper and its Supplementary Information.

Appendix A. Supplementary data

Supplementary material related to this article can be found online.

References

1. Wang Y, Chen X, Zhang H, Xia G, Sun D, Yu X (2020) Heterostructures Built in Metal Hydrides for Advanced Hydrogen Storage Reversibility. Adv Mater 32:1–8. https://doi.org/10.1002/adma.202002647
2. Zhang XL, Liu YF, Zhang X, Hu JJ, Gao MX, Pan HG (2020) Empowering hydrogen storage performance of MgH2 by nanoengineering and nanocatalysis. Mater Today Nano 9. https://doi.org/10.1016/j.mtnano.2019.100064
3. Prinzhofer A, Tahara Cissé CS, Diallo AB (2018) Discovery of a large accumulation of natural hydrogen in Bourakebougou (Mali). Int J Hydrogen Energy 43:19315–19326. https://doi.org/10.1016/j.ijhydene.2018.08.193
4. Rusman NAA, Dahari M (2016) A review on the current progress of metal hydrides material for solid-state hydrogen storage applications. Int J Hydrogen Energy 41:12108–12126. https://doi.org/10.1016/j.ijhydene.2016.05.244
5. He T, Cao H, Chen P (2019) Complex Hydrides for Energy Storage, Conversion, and Utilization. Adv Mater 31:1–19. https://doi.org/10.1002/adma.201902757
6. Lai Q, Sun Y, Wang T, Modi P, Cazorla C, Demirci UB, Ares Fernandez JR, Leardini F, Aguey-Zinsou KF (2019) How to Design Hydrogen Storage Materials? Fundamentals, Synthesis, and Storage Tanks. Adv Sustain Syst 3:1–64. https://doi.org/10.1002/adsu.201900043
7. Castilla-Martinez CA, Moury R, Ould-Amara S, Demirci UB (2021) Destabilization of boron-based compounds for hydrogen storage in the solid-state: Recent advances. Energies 14. https://doi.org/10.3390/en14217003
8. Puszkiel J, Gasnier A, Amica G, Gennari F (2020) Tuning LiBH4 for hydrogen storage: Destabilization, additive, and nanoconfinement approaches. Molecules 25:163–201. https://doi.org/10.3390/molecules25010163
9. Züttel A, Rentsch S, Fischer P, Wenger P, Sudan P, Mauron P, Emmenegger C (2003) Hydrogen storage properties of LiBH4. J Alloys Compd 356–357. 515-520. https://doi.org/10.1016/S0925-8388(02)01253-7
10. Ding Z, Li S, Zhou Y, Chen Z, Yang W, Ma W, Shaw L (2020) LiBH4 for hydrogen storage - New perspectives. Nano Mater Sci 2:109–119. https://doi.org/10.1016/j.nanoms.2019.09.003
11. Orimo SI, Nakamori Y, Eliseo JR, Züttel A, Jensen CM (2007) Complex hydrides for hydrogen storage. Chem Rev 107:4111–4132. https://doi.org/10.1021/cr0501846
12. Hoang K, Van De Walle CG (2012) Mechanism for the decomposition of lithium borohydride. Int J Hydrogen Energy 37:5825–5832. https://doi.org/10.1016/j.ijhydene.2012.01.002
13. Yang J, Sudik A, Wolverton C (2007) Destabilizing LiBH4 with a metal (M = Mg, Al, Ti, V, Cr, or Sc) or metal hydride (MH2 = MgH2, TiH2, or CaH 2). J Phys Chem C 111:19134–19140. https://doi.org/10.1021/jp076434z

14. Vajo JJ, Skeith SL, Mertens F (2005) Reversible storage of hydrogen in destabilized LiBH4. J Phys Chem B 109:3719–3722. https://doi.org/10.1021/jp040769o
15. Huang Z, Wang Y, Wang D, Yang F, Wu Z, Zhang Z (2018) Influence of transition metals Fe, Co, Ni, Cu and Ti on the dehydrogenation characteristics of LiBH4: A first-principles investigation. Comput Theor Chem 1133:33–39. https://doi.org/10.1016/j.comptc.2018.04.017
16. Yu XB, Grant DM, Walker GS (2009) Dehydrogenation of LiBH4 destabilized with various oxides. J Phys Chem C 113:17945–17949. https://doi.org/10.1021/jp906519p
17. Au M, Jurgensen AR, Spencer WA, Anton DL, Pinkerton FE, Hwang SJ, Kim C, Bowman RC (2008) Stability and reversibility of lithium borohydrides doped by metal halides and hydrides. J Phys Chem C 112:18661–18671. https://doi.org/10.1021/jp8024304
18. Li HW, Yan Y, Orimo SI, Züttel A, Jensen CM (2011) Recent progress in metal borohydrides for hydrogen storage. Energies 4:185–214. https://doi.org/10.3390/en4010185
19. Yu X, Tang Z, Sun D, Ouyang L, Zhu M (2017) Recent advances and remaining challenges of nanostructured materials for hydrogen storage applications. Prog Mater Sci 88:1–48. https://doi.org/10.1016/j.pmatsci.2017.03.001
20. Gross AF, Vajo JJ, Van Atta SL, Olson GL (2008) Enhanced hydrogen storage kinetics of LiBH4 in nanoporous carbon scaffolds. J Phys Chem C 112:5651–5657. https://doi.org/10.1021/jp711066t
21. Liu X, Peaslee D, Jost CZ, Majzoub EH (2010) Controlling the decomposition pathway of LiBH4 via confinement in highly ordered nanoporous carbon. J Phys Chem C 114:14036–14041. https://doi.org/10.1021/jp1055045
22. Liu X, Peaslee D, Jost CZ, Baumann TF, Majzoub EH (2011) Systematic pore-size effects of nanoconfinement of LiBH4: Elimination of diborane release and tunable behavior for hydrogen storage applications. Chem Mater 23:1331–1336. https://doi.org/10.1021/cm103546g
23. Gasnier A, Gennari FC (2017) Graphene entanglement in a mesoporous resorcinol-formaldehyde matrix applied to the nanoconfinement of LiBH4 for hydrogen storage. RSC Adv 7. https://doi.org/10.1039/c7ra02288c
24. Suwarno P, Ngene A, Nale TM, Eggenhuisen M, Oschatz JP, Embs A, Remhof PE, De Jongh (2017) Confinement Effects for Lithium Borohydride: Comparing Silica and Carbon Scaffolds. J Phys Chem C 121:4197–4205. https://doi.org/10.1021/acs.jpcc.6b13094
25. Ngene P, Adelhelm P, Beale AM, De Jong KP, De Jongh PE (2010) LiBH4/SBA-15 nanocomposites prepared by melt infiltration under hydrogen pressure: Synthesis and hydrogen sorption properties. J Phys Chem C 114:6163–6168. https://doi.org/10.1021/jp9065949
26. Cahen S, Eymery JB, Janot R, Tarascon JM (2009) Improvement of the LiBH4 hydrogen desorption by inclusion into mesoporous carbons. J Power Sources 189:902–908. https://doi.org/10.1016/j.jpowsour.2009.01.002
27. Gasnier A, Luguet M, Pereira AG, Troiani H, Zampieri G, Gennari FC (2019) Entanglement of N-doped graphene in resorcinol-formaldehyde: Effect over nanoconfined LiBH4 for hydrogen storage. Carbon N Y 147:284–294. https://doi.org/10.1016/j.carbon.2019.02.090

28. Wang S, Gao M, Yao Z, Liu Y, Wu M, Li Z, Liu Y, Sun W, Pan H (2022) A nanoconfined-LiBH4 system using a unique multifunctional porous scaffold of carbon wrapped ultrafine Fe3O4 skeleton for reversible hydrogen storage with high capacity. Chem Eng J 428:131056. https://doi.org/10.1016/j.cej.2021.131056
29. Guo L, Li Y, Ma Y, Liu Y, Peng D, Zhang L, Han S (2017) Enhanced hydrogen storage capacity and reversibility of LiBH4 encapsulated in carbon nanocages. Int J Hydrogen Energy 42:2215–2222. https://doi.org/10.1016/j.ijhydene.2016.11.184
30. Xia G, Tan Y, Wu F, Fang F, Sun D, Guo Z, Huang Z, Yu X (2016) Graphene-wrapped reversible reaction for advanced hydrogen storage. Nano Energy 26:488–495. https://doi.org/10.1016/j.nanoen.2016.06.016
31. Jia Y, Zhou P, Xiao X, Wang X, Han B, Wang J, Xu F, Sun L, Chen L (2024) Synergetic action of 0D/2D/3D N-doped carbon nanocages and NbB2 nanocatalyst on reversible hydrogen storage performance of lithium borohydride. Chem Eng J 485:150090. https://doi.org/10.1016/j.cej.2024.150090
32. Gasnier A, Amica G, Juan J, Troiani H, Gennari FC (2019) Graphene-Rich Aerogels Decorated with Nickel and Cobalt Nanoparticles: Effect on Hydrogen Storage Properties of Nanoconfined LiBH4. J Phys Chem C. https://doi.org/10.1021/acs.jpcc.9b09510
33. Ngene P, Van Zwienen R, De Jongh PE (2010) Reversibility of the hydrogen desorption from LiBH4: A synergetic effect of nanoconfinement and Ni addition. Chem Commun 46:8201–8203. https://doi.org/10.1039/c0cc03218b
34. Zhou H, Wang X, Liu H, Yan M (2017) Enhanced hydrogen storage properties of 2LiBH4-LiAlH4 nanoconfined in resorcinol formaldehyde carbon aerogel. J Alloys Compd 726:525–531. https://doi.org/10.1016/j.jallcom.2017.07.080
35. Gosalawit-Utke R, Milanese C, Javadian P, Jepsen J, Laipple D, Karmi F, Puszkiel J, Jensen TR, Marini A, Klassen T, Dornheim M (2013) Nanoconfined 2LiBH4-MgH2-TiCl3 in carbon aerogel scaffold for reversible hydrogen storage. Int J Hydrogen Energy 38:3275–3282. https://doi.org/10.1016/j.ijhydene.2012.12.123
36. Wang H, Lin HJ, Cai WT, Ouyang LZ, Zhu M (2016) Tuning kinetics and thermodynamics of hydrogen storage in light metal element based systems - A review of recent progress. J Alloys Compd 658:280–300. https://doi.org/10.1016/j.jallcom.2015.10.090
37. Cai W, Wang H, Liu J, Jiao L, Wang Y, Ouyang L, Sun T, Sun D, Wang H, Yao X, Zhu M (2014) Towards easy reversible dehydrogenation of LiBH4 by catalyzing hierarchic nanostructured CoB. Nano Energy 10:235–244. https://doi.org/10.1016/j.nanoen.2014.09.001
38. Cai W, Hou J, Huang S, Chen J, Yang Y, Tao P, Ouyang L, Wang H, Yang X (2019) Altering the chemical state of boron towards the facile synthesis of LiBH4 via hydrogenating lithium compound-metal boride mixture. Renew Energy 134:235–240. https://doi.org/10.1016/j.renene.2018.11.042
39. Mason T, Majzoub EH (2014) Effects of a carbon surface environment on the decomposition properties of nanoparticle LiBH4: A first-principles study. J Phys Chem C 118:8852–8858.

https://doi.org/10.1021/jp409819g

40. House SD, Liu X, Rockett AA, Majzoub EH, Robertson IM (2014) Characterization of the dehydrogenation process of LiBH4 confined in nanoporous carbon. J Phys Chem C 118:8843–8851. https://doi.org/10.1021/jp4098205
41. Martínez AA, Gasnier A, Gennari FC (2022) Pore Filling of a Carbon Matrix by Melt-Impregnated LiBH4. J Phys Chem C 126:66–78. https://doi.org/10.1021/acs.jpcc.1c09158
42. Lambregts SFH, Van Eck ERH, Suwarno P, Ngene PE, De Jongh APM, Kentgens (2019) Phase Behavior and Ion Dynamics of Nanoconfined LiBH4 in Silica. J Phys Chem C 123:25559–25569. https://doi.org/10.1021/acs.jpcc.9b06477
43. Martínez AA, Gasnier A, Gennari FC (2022) From Iron to Copper: The Effect of Transition Metal Catalysts on the Hydrogen Storage Properties of Nanoconfined LiBH4 in a Graphene-Rich N-Doped Matrix. Molecules 27. https://doi.org/10.3390/molecules27092921
44. Garanzini I, Moreno MS, Arneodo P, Gasnier A (2025) International Journal of Hydrogen Energy Metallic gallium: A liquid phase to destabilize nanoconfined LiBH. 4:892–904
45. Lambregts SFH, Van Eck ERH, Ngene P, Kentgens APM (2022) The Nature of Interface Interactions Leading to High Ionic Conductivity in LiBH4/SiO2 Nanocomposites. ACS Appl Energy Mater 5:8057–8066. https://doi.org/10.1021/acsaem.2c00527
46. Liu X, Majzoub EH, Stavila V, Bhakta RK, Allendorf MD, Shane DT, Conradi MS, Verdal N, Udovic TJ, Hwang SJ (2013) Probing the unusual anion mobility of LiBH4 confined in highly ordered nanoporous carbon frameworks via solid state NMR and quasielastic neutron scattering. J Mater Chem A 1:9935–9941. https://doi.org/10.1039/c3ta12051a
47. Masset PJ (2014) Lithium Hydride Solubility in Molten Chlorides. Molten Salts Chem Technol 9781118448:213–218. https://doi.org/10.1002/9781118448847.ch3h
48. Ley MB, Roedern E, Jensen TR (2014) Eutectic melting of LiBH4-KBH4. Phys Chem Chem Phys 16:24194–24199. https://doi.org/10.1039/c4cp03207a
49. Nickels EA, Jones MO, David WIF, Johnson SR, Lowton RL, Sommariva M, Edwards PP (2008) Tuning the Decomposition Temperature in Complex Hydrides: Synthesis of a Mixed Alkali Metal Borohydride **. 2817–2819. https://doi.org/10.1002/anie.200704949
50. Paskevicius M, Jepsen LH, Schouwink P, Černý R, Ravnsbæk DB, Filinchuk Y, Dornheim M, Besenbacher F, Jensen TR (2017) Metal borohydrides and derivatives-synthesis, structure and properties. Chem Soc Rev 46:1565–1634. https://doi.org/10.1039/c6cs00705h

Figures

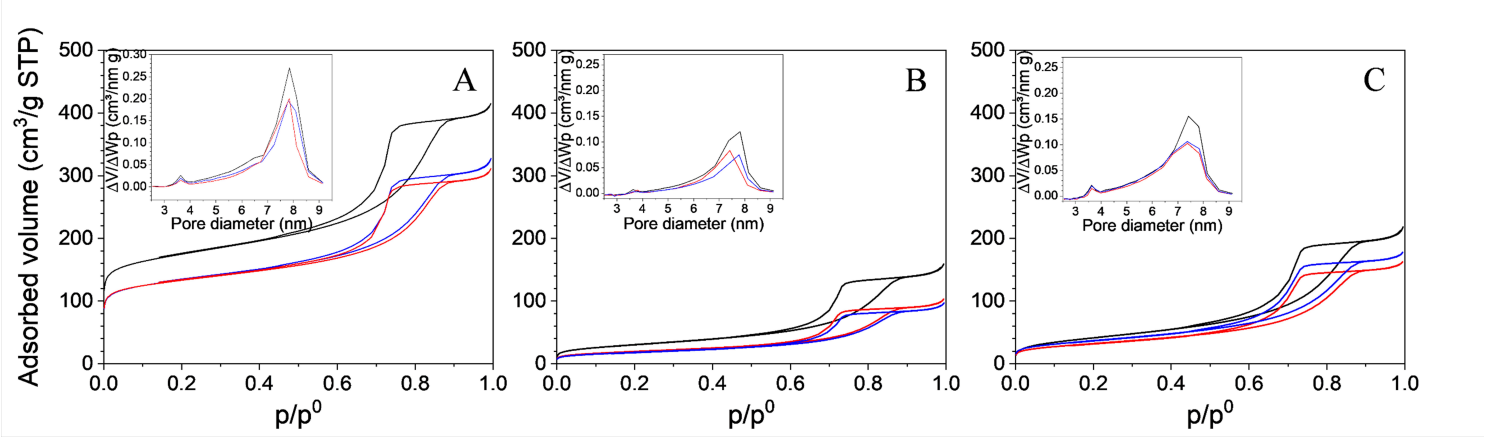


Figure 1

Nitrogen isotherms of R (black), ${}^{w}R_E$ (red), and ${}^{g}R_E$ (blue) matrices, before impregnation (A), after filling with $LiBH_4$ 56 vol% (B), and after cycle dehydrogenation (C). Inset: pore volume distribution according to the BJH model.

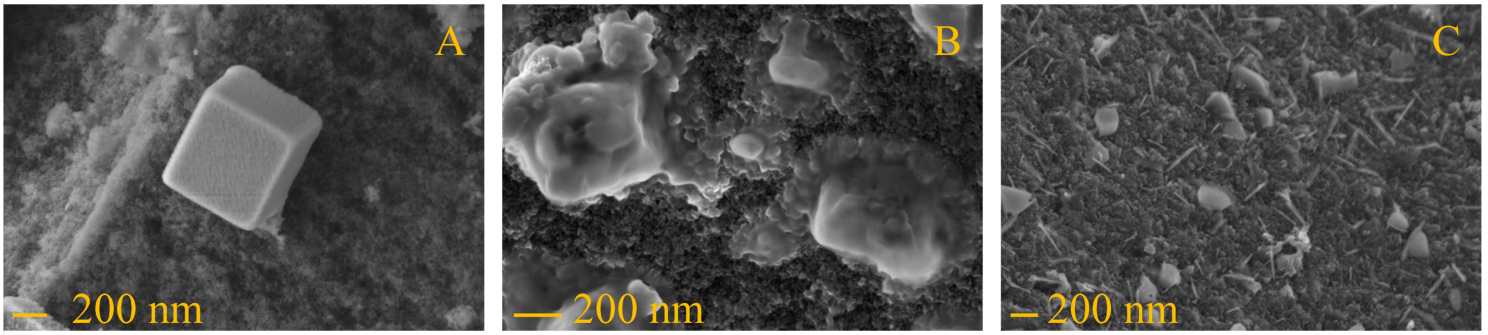


Figure 2

SEM observations of ${}^{w}R_E$ before filling (A), after filling at 56% with $LiBH_4$ (B), and after cycling (C).

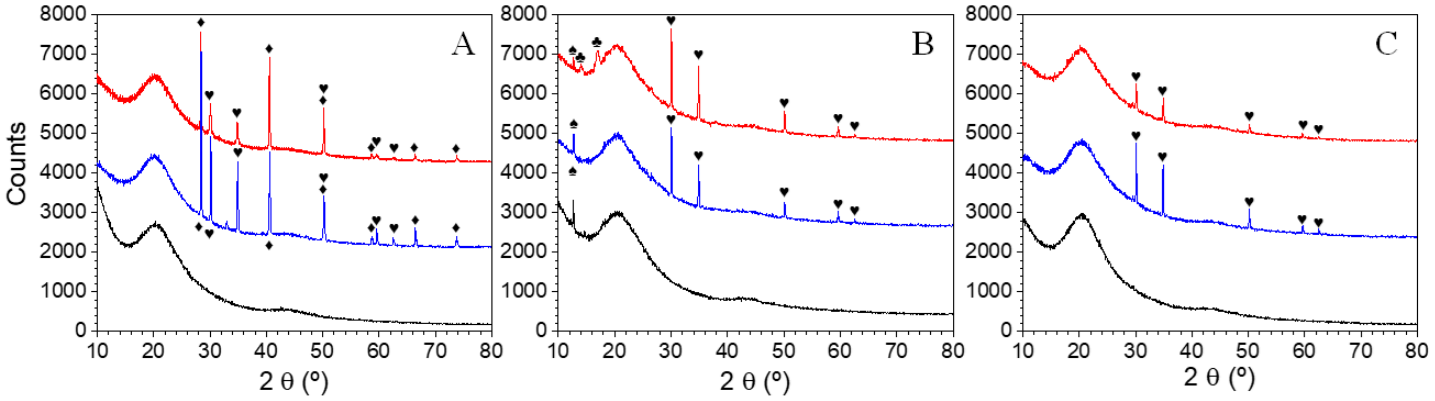


Figure 3. XRD trace of R (black), ${}^{g}R_E$ (blue), and ${}^{w}R_E$ (red) matrices before impregnation (A), after filling with $LiBH_4$ 56 vol% (B), and after cycle dehydrogenation (C). Peak attribution: ♦=KCl,♥=LiCl, ♠=$LiBH_4$, ♣=$LiK(BH_4)_2$.

Figure 3

See image above for figure legend

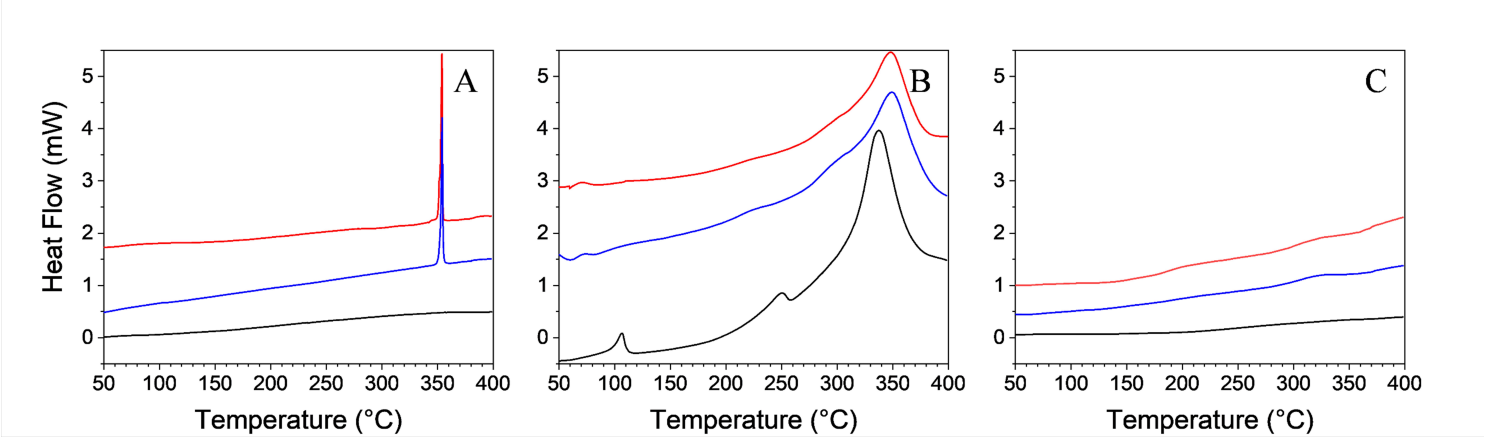


Figure 4

DSC of R (black), ${}^{g}R_E$ (blue), and ${}^{w}R_E$ (red) matrices before impregnation (A), after filling with $LiBH_4$ 56 vol% (B), and after cycle dehydrogenation (C).

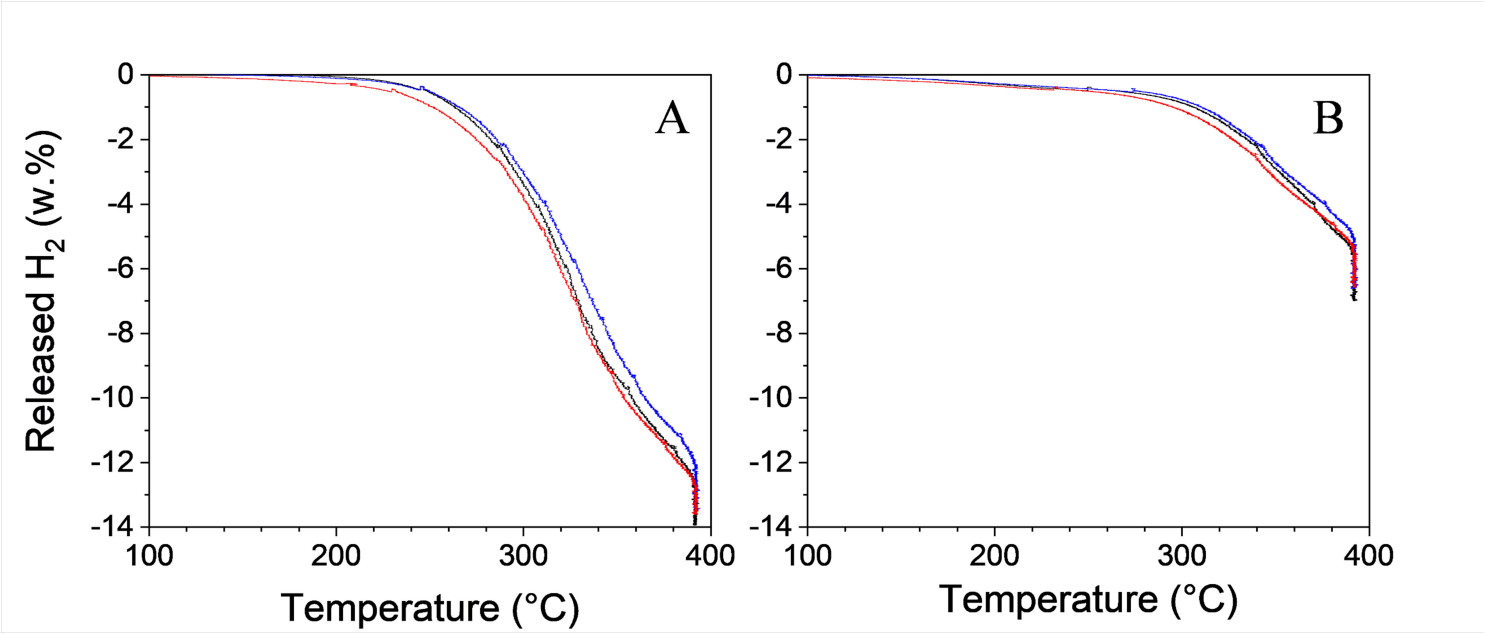


Figure 5

Volumetric studies presenting the first (A) and second (B) dehydrogenation of R^{56} (black), ${}^{g}R_E^{56}$ (blue), and ${}^{w}R_E^{56}$ (red).

Supplementary Files

This is a list of supplementary files associated with this preprint. Click to download.

- 2026NanotechnolEnvironEngSIAnonymised.docx